VI International Conference on Computational Methods for Coupled Problems in Science and Engineering
COUPLED PROBLEMS 2015
B. Schrefler, E. Oñate and M. Papadrakakis (Eds)

NUMERICAL METHODS IN SIMULATION OF RESISTANCE WELDING

CHRIS V. NIELSEN[1*], PAULO A.F. MARTINS[2], WENQI ZHANG[3] AND NIELS BAY[1†]

[1] Department of Mechanical Engineering, Technical University of Denmark
Produktionstorvet 425, 2800 Kgs. Lyngby, Denmark
[*]e-mail: cvni@mek.dtu.dk [†]e-mail: nbay@mek.dtu.dk

[2] Instituto Superior Tecnico, Universidade de Lisboa
Av. Rovisco Pais, 1049-001 Lisboa, Portugal
e-mail: pmartins@tecnico.ulisboa.pt

[3] SWANTEC Software and Engineering ApS
Diplomvej 373, 2800 Kgs. Lyngby, Denmark
e-mail: wz@swantec.com

Key words: Resistance Welding, Finite Element Method, Electro-Thermo-Mechanical, Phase Changes, Hardness, Damage.

Abstract. Finite element simulation of resistance welding requires coupling between mechanical, thermal and electrical models. This paper presents the numerical models and their couplings that are utilized in the computer program SORPAS. A mechanical model based on the irreducible flow formulation is utilized to simulate plastic deformation and the resulting distribution of stress, a thermal model based on transient heat transfer is used to determine the distribution of temperature, and a steady-state electrical model is employed to calculate the distribution of electrical potential and current density. From a resistance welding point of view, the most essential coupling between the above mentioned models is the heat generation by electrical current due to Joule heating. The interaction between multiple objects is another critical feature of the numerical simulation of resistance welding because it influences the contact area and the distribution of contact pressure. The numerical simulation of resistance welding is illustrated by a spot welding example that includes subsequent tensile shear testing.

1 INTRODUCTION

Resistance welding is a widely applied joining technology. Spot welding, one of its variants, is very important in automotive assembly lines as it is a robust and effective joining process that is under continuous development to meet new demands due to novel materials, complex welding geometries and quality requirements. Projection welding is another widely applied variant of resistance welding which benefits from natural or fabricated projections.

Numerical simulation methods applied to resistance welding can provide a better understanding of the joining process and be utilized in the definition of operating parameters and prediction of the final quality of the welds. The role of numerical simulation in resistance welding is stated well by Singh [1], who points out that simulation cannot replace or substitute ingenuity or creativeness, but it can help in gaining understanding of the process, and hence reduce the amount of time spent during development.

During the 1960s and 1970s, the first models considering resistance welding were exclusively focused on the temperature history and made use of 1D or 2D axisymmetric models without mechanical coupling. Early numerical simulations of resistance welding, starting in the 1980s, include finite element analysis by Nied [2] and application of the finite difference method by Cho and Cho [3]. The finite element method is more suited for the analysis of resistance welding due to the deformations involved in the process. Nied [2], who used the commercial program ANSYS, is recognized as the first to apply finite element analysis to resistance welding. He setup a rather complete model to study resistance spot welding that included electro-thermo-mechanical discretization of the electrodes and workpieces by solid elements and by surface elements at the interfaces between objects to account for elastic mechanical contact (Herzian contact) and for electrical and thermal contact resistances. Although the simulation only considered elastic deformation, it was the first ever to consider the developing contact areas that play a key role in the process. Furthermore, good agreement between presented experiments and simulations provided motivation and inspiration for others to continue developments of numerical methods applied to resistance welding.

Another example of finite elements applied to resistance welding is the numerical modelling of projection welding of an automotive door hinge with two projections welded to a sheet that was performed by Zhu et al. [4] using ANSYS with an electro-thermo-mechanical coupled model that included plastic deformation. Other examples are given by Ma and Murukawa [5].

The objective of this paper is to present an overview of the numerical methods utilized in the commercial finite element program SORPAS for the complete simulation of resistance welding. The program was developed in the 1990s at the Technical University of Denmark to solve 2D industrial applications and later commercialized, maintained and further developed by SWANTEC Software and Engineering [6, 7]. In contrast to general purpose finite element computer programs, SORPAS is a special purpose software dedicated to simulation and optimization of resistance welding processes. The 3D version of SORPAS has been recently developed in collaborative partnership between the Technical University of Denmark, the University of Lisbon and SWANTEC Software and Engineering and has been commercialized since 2012.

The paper is organized such that Section 2 includes basic numerical models and the necessary couplings in the electro-thermo-mechanical model. Section 3 presents the numerical contact implementation as well as the physical contact modeling that are crucial for the simulation of resistance welding. Section 4 describes the prediction of phase changes and resulting hardness related to the weld quality. Section 5 presents a resistance welding example showing the application of the numerical methods to process simulation and subsequent strength test simulation, and Section 6 concludes.

2 ELECTRO-THERMO-MECHNICAL NUMERICAL MODEL

This section presents the mechanical, thermal and electrical formulations that give support to the associated software modules and describes the necessary couplings. Coupled damage modeling is included as part of the mechanical module, while couplings between the three core modules are covered subsequently together with material dependencies.

2.1 Mechanical module

The mechanical module is based on the irreducible flow formulation, which takes the following weak variational form,

$$\int_V \bar{\sigma}\delta\dot{\bar{\varepsilon}}\,dV + K\int_V \dot{\varepsilon}_{ii}\delta\dot{\varepsilon}_{jj}\,dV - \int_{S_t} t_i\delta u_i\,dS + \delta\Pi_C = 0 \tag{1}$$

where the first term covers the energy rate due to plastic deformation in domain volume V, the second term imposes the incompressibility constraint, the third term applies surface tractions over surface S_t and the fourth term is due to the contact contribution to be described in Section 3.1. Variations with respect to velocities u_i are identified by δ while $\bar{\sigma}$ is the effective stress, $\dot{\bar{\varepsilon}}$ is the effective plastic strain rate, the penalty factor K is a large positive number, $\dot{\varepsilon}_{ii}$ is the volumetric strain rate, and t_i are prescribed surface tractions.

The plastic deformation is generally assumed to follow the isotropic von Mises yield criterion,

$$\bar{\sigma}^2 = 3J_2 \tag{2}$$

where J_2 is the second invariant of the deviatoric stress tensor σ'_{ij}. When simulating quasi-static mechanical strength tests the accumulation of damage is accounted for by utilizing constitutive equations of metallic materials with porosity. The formation of porosity is associated with generation and coalescence of voids in average terms over each element. The yield criterion,

$$\bar{\sigma}_R^2 = AJ_2 + BI_1 \tag{3}$$

where I_1 is the first invariant of the stress tensor σ_{ij}, is capable of handling the volumetric changes due to variations in relative density. The effective stress response $\bar{\sigma}_R$ for a given relative density R is given by $\bar{\sigma}_R^2 = C\bar{\sigma}^2$, where $\bar{\sigma}$ is the effective stress response of the fully dense material. The material constants A, B and C are dependent on the relative density and are assumed to follow the porous plasticity theory by Shima and Oyane [8]. The constant $C = \dfrac{R^5}{1+(2.49/3)^2(1-R)^{1.028}} \le 1$ is responsible for the decrease in flow stress when the relative density decreases ($R \le 1$). The accumulated damage D is formulated as,

$$D = 1 - R \tag{4}$$

This expression is zero for fully dense materials and increases linearly with decreasing relative density.

2.2 Thermal module

The thermal module is based on the classical Galerkin treatment of the heat transfer equation giving the following governing equation for the temperature T ,

$$\int_V kT_{,i}\delta T_{,i}\,dV + \int_V \rho_m c_m \dot{T}\delta T\,dV - \int_V \dot{q}_V \delta T\,dV - \int_S \dot{q}_S dS + \delta\Pi_T = 0 \tag{5}$$

where the first term is due to heat conduction, the second term is due to stored energy associated with a temperature rate $\dot{T}$, the third term includes the heat generation rate in the volume $\dot{q}_V$ and the fourth term covers the rate of heat generation (or loses) at the surface $\dot{q}_S$. The last term includes thermal contact between objects as described in Section 3.2.

In equation (5), k is the thermal conductivity, ρ_m is the mass density, c_m is the heat capacity, and δ is used for the arbitrary variations with respect to temperature.

The contributions to $\dot{q}_V$ stem from plastic work and Joule heating, as follows,

$$\begin{aligned} \dot{q}_{plastic} &= \beta\overline{\sigma}\dot{\overline{\varepsilon}} \\ \dot{q}_{Joule} &= \rho J^2 \end{aligned} \tag{6}$$

where β is the fraction of mechanical energy transformed into heat and is usually assumed to be in the range between 0.85 to 0.95, ρ is the electrical resistivity and J is the current density calculated in the electrical module (Section 2.3).

The rate of heat generation $\dot{q}_S$ along surfaces is due to friction, convection and radiation, where the latter two are heat loses during the welding process,

$$\begin{aligned} \dot{q}_{friction} &= \tau_f |v_r| \\ \dot{q}_{convection} &= -h\left(T_s - T_f\right) \\ \dot{q}_{radiation} &= -\varepsilon_{emis}\sigma_{SB}\left(T_s^4 - T_f^4\right) \end{aligned} \tag{7}$$

In the above equations, the heat due to friction is obtained from the product of the friction shear stress τ_f and the relative sliding speed v_r between two surfaces in contact. The convection is associated with the heat transfer coefficient h, the surface temperature T_s and the temperature T_f of the surroundings. The parameters expressing the radiation are the emissivity coefficient ε_{emis} and the Stefan-Boltzmann constant σ_{SB} .

2.3 Electrical module

The electric potential Φ is the major variable in the electrical module. The governing equation is the Laplace equation, which for an arbitrary variation of the electric potential $\delta\Phi$ and application of the divergence theorem can be written as,

$$\int_V \Phi_{,i}\delta\Phi_{,i}dV - \int_S \Phi_{,n}dS + \delta\Pi_\Phi = 0 \tag{8}$$

with the addition of the last term accounting for electrical contact between objects to be presented in Section 3.2. Equation (8) simplifies by the cancellation of the second term

because of the gradient of the potential along free surfaces $\Phi_{,n}$ being zero.

As it was early stated by Greenwood and Williamson [9], the electric field has a much faster reaction rate than the temperature field, and therefore the steady state approximation, $\dot{\Phi} = 0$, behind (8) is generally considered a very good approach. This means that the electric potential is determined solely by geometry.

The current density J is available from the ratio of the potential gradient and the electrical resistivity, $J_i = \Phi_{,i} / \rho$.

2.4 Electro-thermo-mechanical couplings

The three modules are coupled as schematically shown by Figure 1. The mechanical module is run at the beginning of each step to establish the velocity field and geometry change, the contact areas and the overall stress response. Besides the new geometry, the direct influences in other modules are the deformation heat (6) and friction generated heat (7) in the thermal module. Another important influence is on the electrical and thermal contact properties that depend on the contact stresses.

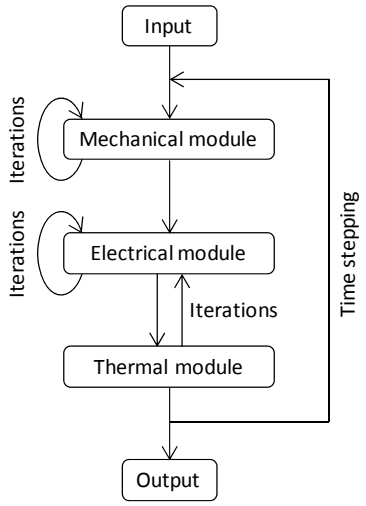

Figure 1: Numerical couplings between the electro-thermo-mechanical simulation of resistance welding.

After convergence of the mechanical module, the electrical and thermal modules are run until individual and mutual convergence. The output from the electrical module is the current density giving rise to Joule heating (6) characterizing the resistance welding process. The resulting temperatures in the thermal module are used to update all temperature dependent material properties. Among the most important influences by the material property updates are the mechanical softening, the increasing electrical resistivity and the changes in thermal properties themselves.

The coupling with the mechanical module is weaker than the coupling between the electrical and thermal modules. This is justified by simulating with very small time steps ensuring that the error in the mechanical module due to temperatures of the previous step is minimal. On the other hand, the time savings by weakening the coupling to the mechanical module is large. The coupling between the electrical and thermal modules is relatively

cheaper due to having only one third (in 3D) of the degrees of freedom for the two scalar fields (potential and temperature) and due to the linear and inexpensive solution of the electrical module. The limitation to using very small time steps is natural in resistance welding in order to capture all physical effects of the welding process. When, for example, simulating 50 Hz alternating current (AC), each half period corresponds to 10 ms and a minimum number of ten simulation points along each half period therefore requires time steps of maximum 1 ms. The time step should preferably be even smaller, especially when noting that alternating current in resistance welding machines typically has a conduction angle ranging from 50-90% (meaning that only 50-90% of the half period is active, and hence the time step should also be scaled to 50-90% to have the same resolution of the active current profile). Further details of the numerical implementation can be found elsewhere [10].

3 CONTACT

The contact implementation is based on the penalty method with identification of contact pairs by a two-pass node-to-face algorithm. The faces in the contact pairs are quadrilateral surface elements of the hexahedral volume meshes of the objects. The normal directions in the contact pairs are determined uniquely by one of the four triangles appearing when introducing a temporary center node in the quadrilateral surface element. The choice of the triangle is determined by the projection point of the contacting node. This method was also adopted by Doghri et al. [11] to overcome symmetry loss that appear with the alternative, and not unique, division of the quadrilateral surface into two triangles by one of the two diagonals.

3.1 Mechanical contact

The last term in Equation (1) due to mechanical contact by the penalty method is given by

$$\delta\Pi_C = P\sum_{c=1}^{N_c} g_n^c \delta g_n^c + P\sum_{c=1}^{N_c} g_t^c \delta g_t^c \tag{9}$$

which selectively penalizes normal gap velocities g_n^c by the first term and tangential gap velocities g_t^c by the second term. The penalty factor P is a large positive number applied to N_c contact pairs. The first term is selective in the sense that it is generally active when otherwise leading to penetration and inactive when the two contacting surfaces are separating. However, in contact pairs identified as already welded, the term is always active. The second term is likewise active in welded contact pairs and also when simulating full sticking conditions. During frictionless or frictional sliding, the second term is inactive.

The frictional stress τ_f during frictional sliding is applied in the contact pairs as surface tractions by the third term in (1) and is modeled by a combination of the Amonton-Coulomb law, $\tau_f = \mu\sigma_n$, and the law of constant friction, $\tau_f = mk$ where μ is the friction coefficient, m is the friction factor, σ_n is the normal pressure and k is the shear flow stress. Using the von Mises yield criterion, the flow stress is $\sqrt{3}k$, and the relation $\mu = m/\left(\sqrt{3}a\right)$ between the two friction laws is therefore valid when the transition between the two models take place at a normal pressure normalized by the flow stress $a = \sigma_n/\left(\sqrt{3}k\right)$, where a is typically 1.5 to 3.

The frictional stress is applied in the direction opposite to the relative sliding velocity $\mathbf{v}_r$ through the following expression by Chen and Kobayashi [12],

$$\tau = -\frac{2}{\pi}\tau_f \cdot \arctan\left(\frac{\mathbf{v}_r}{v_0}\right) \tag{10}$$

where the 'arctan' function is introduced to ensure a continuous derivative for the finite element implementation. It resembles the direction sufficiently fine when v_0 is an arbitrary constant much smaller than the relative speed. The surface integration of (10) over each contact element face is performed by 5x5 Gauss quadrature following Barata Marques and Martins [13] who applied the procedure to contact between finite elements and rigid tools.

3.2 Electrical and thermal contact

The numerical contact ensuring the same potential and temperature on both sides of contact interfaces are described by the following two penalty terms,

$$\begin{aligned} \delta\Pi_\Phi &= P\sum_{c=1}^{N_c}\Phi_d^c\delta\Phi_d^c \\ \delta\Pi_T &= P\sum_{c=1}^{N_c}T_d^c\delta T_d^c \end{aligned} \tag{11}$$

by penalization of potential difference Φ_d^c and temperature difference T_d^c in the N_c contact pairs. The two terms are added in equations (8) and (5), respectively.

Physical contact in the electrical and thermal modules is included through thin layers of elements on the object surfaces. The electrical contact resistivity is higher than the bulk resistivities of the two contacting surfaces due to current restriction and eventual surface contaminants such as oil, dirt and grease. The contact resistivity in SORPAS is modeled as follows [7],

$$\rho_c = \frac{3\sigma_{soft}}{\sigma_n}\left(\frac{\rho_1+\rho_2}{2}+\rho_{contaminant}\right) \tag{12}$$

with the fraction of real contact area to the apparent area in front of the parenthesis being expressed through the flow stress of the softer material σ_{soft} and the contact normal pressure σ_n, as also performed by Bowden and Tabor [14]. The fraction of real contact area describes, in conjunction with the two bulk resistivities of the materials in contact ρ_1 and ρ_2, the overall current restriction. The additional resistance due to contaminants is included through the resistivity $\rho_{contaminant}$. The high electrical contact resistivity expressed by (12) is one of the main contributions to the heat generation by Joule heating as it enters in Equation (6).

Thermal contact resistivity is formulated in a similar way with the exception that the thermal resistance of the surface contaminants is considered negligible. Hence, the thermal contact resistance κ_c is expressed through the ratio of real contact area to the apparent area and the average thermal resistance (inverse conductivity) of the two materials, κ_1 and κ_2,

$$\kappa_c = \frac{3\sigma_{soft}}{\sigma_n}\frac{\kappa_1 + \kappa_2}{2} \tag{13}$$

4 PHASE CHANGES AND HARDNESS PREDICTION

The phase changes during resistance welding involve melting and solidification as well as metallurgical changes of the solid materials due to microstructural changes. Besides the changing material properties of the solid or molten material, the latent heat L also needs to be taken into account when simulating in the temperature range between the solidus temperature T_{sol} and the liquidus temperature T_{liq}. The latent heat is included by replacing the heat capacity in (5) by an effective heat capacity $\widetilde{c}_m$ [15],

$$\widetilde{c}_m = c_m + \frac{L}{T_{liq} - T_{sol}} \tag{14}$$

Another effect of melting that needs to be taken into account is volume mixing of material properties when molten materials of different objects contribute to a molten volume.

As regards microstructural phase changes, the following is based on typical automotive steel grades. Austenitization is considered during heating without consideration of the temperature rate such that zero austenite is formed below the Ac1 temperature, 100% austenitization is assumed above the Ac3 temperature and linear interpolation is assumed between the Ac1 and the Ac3 temperatures. Formation of subsequent phases upon cooling takes the formed austenite as the starting point and is then calculated based on critical cooling rates as defined in the continuous cooling transformation (CCT) diagram of Figure 2. The critical cooling rates v_M for formation of martensite, v_B for formation of bainaite and v_{FP} for formation of ferrite/pearlite are calculated from the chemical compositions by the formulas presented by Blondeau et al. [16].

The hardness of each of the phases are calculated by the formulas given in the work by Maynier et al. [17] based on the chemical compositions and the actual cooling rates calculated in the finite element simulations. Having calculated the fractions of each of the phases together with their hardness, the total hardness of the material is calculated by applying volume mixing.

The change in hardness due to the temperature history is taken into account by scaling the flow stress curves approximated by $\bar{\sigma} = C(\varepsilon_0 + \bar{\varepsilon})^n$, where the pre-strain ε_0 and strain hardening exponent n of the original flow stress curve are kept constant while scaling the factor C. The scaling is performed with the objective of obeying the new tensile strength that can be approximated based on the new hardness. A number of simplified analytical approaches as well as empirical relations between the tensile strength and the hardness are available in literature, e.g. [18-21]. The often applied relation, $\sigma_{TS} = 3H_V$, is utilized in SORPAS, where σ_{TS} is the nominal tensile stress at the instability point corresponding to an effective strain $\bar{\varepsilon}_{inst} = n - \varepsilon_0$ and H_V is the Vickers hardness, which is calculated in the finite element simulation as explained above. Introducing the relation between the flow stress curve

(expressing the true stress) and the nominal tensile stress results in the following relation between the (true) flow stress at instability and the hardness,

$$\sigma_{inst} = 3e^{n-\varepsilon_0} H_V \tag{15}$$

which needs to be obeyed for the corresponding effective strain $n-\varepsilon_0$, and hence the new C-value becomes,

$$C = 3e^{n-\varepsilon_0} H_V / n^n \tag{16}$$

The new flow stress curves due to the calculated hardness distribution influence the simulation of strength testing.

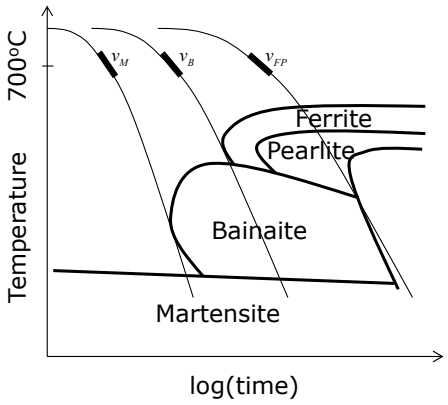

Figure 2: Schematic CTT diagram with indication of critical cooling rates at 700°C for formation of martensite, bainaite and ferrite/pearlite.

5 RESISTANCE SPOT WELDING AND TENSILE SHEAR STRENGTH TESTING

This section presents an example of a resistance spot welding experiment that includes subsequent tensile shear testing up to failure. The simulation is compared to the corresponding experiment to show the capabilities of the finite element implementation in prediction of overall morphology and quality of the weld. Figure 3 includes sheet dimensions, sheet material, electrode type, welding parameters and tensile shear testing speed and direction. The tensile shear testing is in compliance with the ISO standard 14273:2000(E). The initial finite element mesh utilizing one symmetry plane is shown in Figure 3, where the thin layers of elements on both sides of the sheets take into account the coating and interface properties. The electrodes are modeled during the welding simulation but are automatically removed before the tensile shear test simulation.

Experimental and simulated results are included in Figures 4 and 5. The simulated weld nugget diameter is 6.8mm (Figure 4a at the end of the welding time) in comparison with the experimentally observed diameter 6.9mm (Figure 4b). The final shape after tensile shear testing can be compared in Figure 4b and Figure 4c, where the latter includes the simulated damage according to Equation (4). The agreement with the located crack initiation observed in the experiment is good. Both simulation and experiments show full plug failure in the tensile shear tests. Figure 4e shows photographs of the spot weld after failure in one of the

experiments. Figure 4d shows the simulated hardness Vickers that is influencing the tensile shear test simulation by the scaling of the flow stress curves according to Equation (16).

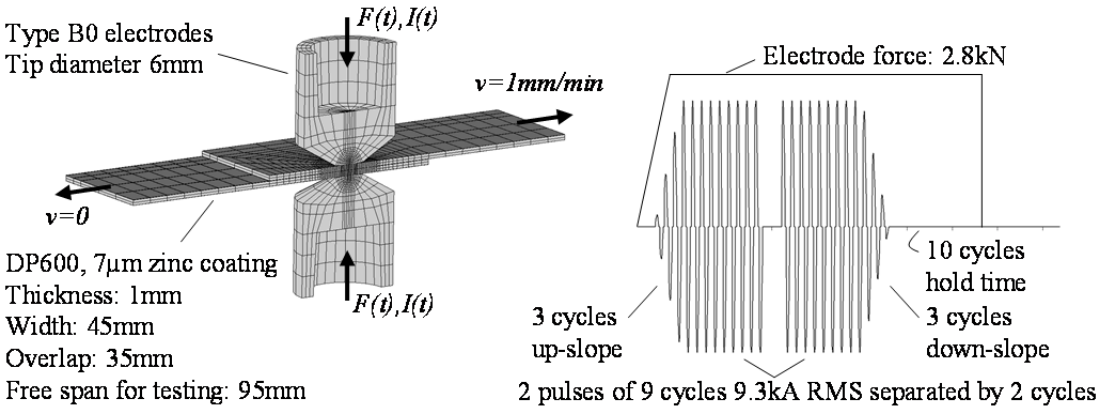

Figure 3: Resistance spot welding case represented by the initial finite element mesh and the welding parameters in terms of electrode force F and welding current I as function of process time t. Subsequent tensile testing velocity is denoted v.

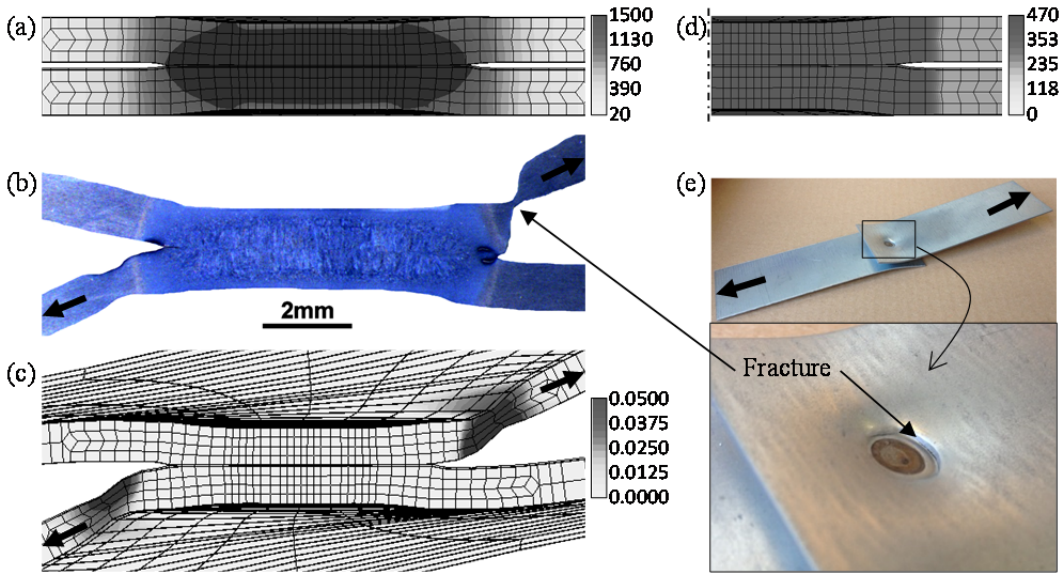

Figure 4: Simulation and experiments. (a) Simulated peak process temperature [°C] during welding and resulting weld nugget. (b) Experimental cross-section after welding and tensile shear testing. (c) Simulated deformation and damage resulting from tensile shear testing. (d) Simulated hardness Vickers distribution. (e) Photographs of spot weld after tensile shear testing until failure. (b,c,e) Arrows identify loaded sheets.

Figure 5 shows the final results of the tensile shear test simulation together with the results of five repetitions of the same experiment. The level of maximum load is captured by the implemented damage model, which is of most industrial relevance, while the sudden drop in load due to fracture does not appear in the simulation due to absence of crack propagation in the finite element model. Good agreement between the simulation and the experiments are observed in the prediction of the tensile shear strength.

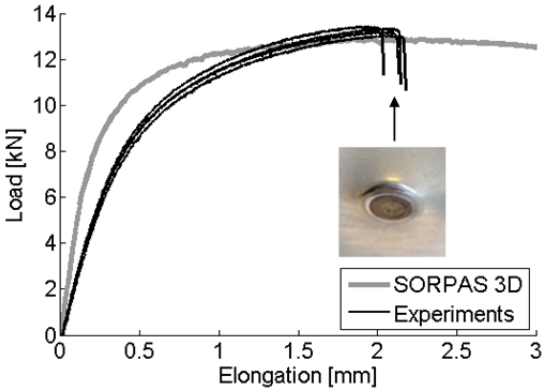

Figure 5: Comparison of simulation and experiments by load-elongation curves for tensile shear testing [22].

6 CONCLUSIONS

The individual modules of the electro-thermo-mechanical finite element implementation in SORPAS 3D and the necessary couplings as well as the level of coupling were comprehensively described. Accurate modeling of contact, phase changes, hardness prediction and resulting new strength of the material in the welded zone allows simulation to be extended into the post-welding destructive tests that are commonly employed to evaluate the overall quality and strength of the resulting weld nuggets.

Comparisons of the weld nugget size, weld strength and failure mode in a test case consisting of a single spot weld of two high strength steels are included to show the overall good agreement between experimental values and observations and numerical predictions.

REFERENCES

[1] Singh, S. Can simulation of the welding process help advance the state of the art in resistance welding? Proceedings of the 3rd International Seminar on: Advances in Resistance Welding, Berlin, Germany, (2012):5-11.

[2] Nied, H.A. The finite element modeling of the resistance spot welding process. Welding Research Supplement (1984) 63(4):123-132.

[3] Cho, H.S. and Cho, Y.J. A study of the thermal behavior in resistance spot welds. Welding Journal (1989) 68(6):236s-244s.

[4] Zhu, W.-F., Lin, Z., Lai X.-M. and Luo, A.-H. Numerical analysis of projection welding on auto-body sheet metal using a coupled finite element method. International Journal of Advanced Manufacturing Technology (2006) 28(1-2):45-52.

[5] Ma, N. and Murukawa, H. Numerical and experimental study on nugget formation in resistance spot welding for three pieces of high strength steel sheets. Journal of Materials Processing Technology (2010) 210:2045-2052.

[6] Zhang, W. and Kristensen, L. Finite element modeling of resistance spot and projection welding processes. The 9th International Conference on Computer Technology in Welding, Detroit, Michigan, (1999):15-23.

[7] Zhang, W. Design and implementation of software for resistance welding process

simulations. Trans. J. Mater. Manuf. (2003) 112(5):556–564.
[8] Shima, S. and Oyane, M. Plasticity theory for porous metals. International Journal of Mechanical Sciences (1976) 18(6):285-291.
[9] Greenwood, J.A. and Williamson, J.B.P. Electrical conduction in solids II. Theory of temperature-dependent conductors. In: Proceedings of the Royal Society of London, Series A, Mathematical and Physical Sciences (1958) 246:13-31.
[10] Nielsen, C.V., Zhang, W., Alves, L.M., Bay, N. and Martins, P.A.F. Modeling of Thermo-Electro-Mechanical Manufacturing Processes with Applications in Metal Forming and Resistance Welding, Springer, (2012).
[11] Doghri, I., Muller, A. and Taylor, R.L. A general three-dimensional contact procedure for implicit finite element codes. Engineering Computations (1998) 15(2):233-259.
[12] Chen, C. and Kobayashi, S. Rigid plastic finite element analysis of ring compression. Application of numerical methods in forming processes, AMD 28, ASME, New York, (1978):163-174.
[13] Barata Marques, M.J.M. and Martins, P.A.F. Three-dimensional finite element contact algorithm for metal forming. International Journal for Numerical Methods in Engineering (1990) 30:1341-1354.
[14] Bowden, F.P. and Tabor, D. The Fabrication and Lubrication of Solids, Oxford University Press, (1950).
[15] Zhang, W., Jensen, H.H. and Bay, N. Finite element modeling of spot welding similar and dissimilar metals. The 7th International Conference on Computer Technology in Welding, San Francisco, USA, (1997):364-373.
[16] Blondeau, R., Maynier, P., Dollet, J. and Vieillard-Baron, B. Prévision de la dureté, de la résistance et de la limite d'elasticité des aciers au carbone et faiblement alliés d'après leur composition et leur traitement thermique. Mémoires Scientifiques Revue Métallurgie (1975):759-769.
[17] Maynier, P., Jungmann, B. and Dollet, J. Creusot-Loire system for the prediction of the mechanical properties of low alloy steel products. Hardenability Concepts with Applications to Steels. The Metallurgical Society of AIME Heat Treatment Committee / American Society for Metals Activity on Phase Transformations (1978):518-545.
[18] Tabor, D. The physical meaning of indentation and scratch hardness. British Journal of Applied Physics (1956) 7:159-166.
[19] Cahoon J.R. An improved equation relating hardness to ultimate strength. Metallurgical Transactions (1972) 3:3040.
[20] Busby, J.T., Hash, M.C. and Was, G.S. The relationship between hardness and yield stress in irradiated austenitic and ferritic steels. Journal of Nuclear Materials (2005) 336:267-278.
[21] Pavlina, E.J. and Van Tyne, C.J. Correlation of yield strength and tensile strength with hardness for steels. Journal of Materials Engineering and Performance (2008) 17(6):888-893.
[22] Nielsen, C.V., Bennedbæk, R.A.K., Larsen, M.B., Bay, N., Chergui, A., Zhang, W. and Martins, P.A.F. Experimental and simulated strength of spot welds. The 8th International Seminar on Advances in Resistance Welding, Baveno, Italy, (2014): 161-172.